## EDGE ARTICLE

Check for updates

# δ-VOPO₄ as a high-voltage cathode material for aqueous zinc-ion batteries†

Dong Zhao,[a] Xiangjun Pu,*[b] Shenglong Tang,[a] Mingyue Ding, [ID] *[a] Yubin Zeng,[a] Yuliang Cao [ID] [b] and Zhongxue Chen [ID] *[a]

Aqueous zinc-ion batteries (AZIBs) with excellent safety, low-cost and environmental friendliness have great application potential in large-scale energy storage systems and thus have received extensive research interest. Layered oxovanadium phosphate dihydrate (VOPO₄·2H₂O) is an appealing cathode for AZIBs due to the unique layered framework and desirable discharge plateau, but bottlenecked by low operation voltage and unstable cycling. Herein, we propose delta-oxovanadium phosphate (δ-VOPO₄) without conventional pre-embedding of metal elements or organics into the structure and paired it into AZIBs for the first time. Consequently, superior to the layered counterpart, δ-VOPO₄ exhibits better performance with a prominent discharge voltage of 1.46 V and a higher specific capacity of 122.6 mA h g⁻¹ at 1C (1C = 330 mA g⁻¹), as well as an impressive capacity retention of 90.88 mA h g⁻¹ after 1000 cycles under 10C. By investigation of structure resolution and theoretical calculation, this work well elucidates the structure–function relationship in vanadyl phosphates, offering more chances for exploration of new cathode materials to construct high performance AZIBs.

## Introduction

Facing the shortage of fossil energy and greenhouse effect, development and utilization of sustainable energy is one of the global challenges.[1,2] The successful application of lithium-ion batteries (LIBs) in industries for portable electronic devices and electric vehicles provides an electrochemical solution to this dilemma.[3] However, the long-term utilization of LIBs is restricted by high cost, limited resources, poor thermal stability from organic electrolytes and strict assembly conditions.[4] Aqueous multivalent metal-ion batteries especially aqueous zinc-ion batteries (AZIBs) inherent with non-flammability of water could merge this gap between high specific capacity and excellent safety.[5,6] They have been widely studied due to the high volumetric energy density and abundant zinc reserves.[7]

At present, the cathode material is the bottleneck limiting the energy density of AZIBs due to the limited specific capacity compared to that of Zn metal anodes. Typical cathode materials for aqueous zinc-ion batteries include manganese-based materials, Prussian blue analogs and vanadium-based materials. Among them, manganese-based compounds inevitably suffer

from manganese dissolution and structure destruction due to the Jahn–Teller effect when Mn³⁺ is formed. In addition, the competition mechanism embedded by H⁺ and Zn²⁺ is still controversial.[8,9] Prussian blue materials have low electrical conductivity, and limited first-cycle efficiency and cycling life, which restrict their further development. Vanadium-based materials are widely studied in virtue of multi-valence changes and compositional structures. However, vanadium oxides and vanadates have low operating voltages and always undergo a large irreversible deformation during the process of Zn²⁺ intercalation, which is detrimental to long-term cycling stability. Therefore, it is urgent and significant to exploit and develop novel cathode materials.

Among various chemistry systems, vanadium-based phosphates have advantages of high theoretical capacity, open structural framework and high operating voltage, and stand out as potential candidates for AZIBs.[10,11] Indeed, they have been proved to have excellent performance in lithium and sodium ion batteries and have potential for large-scale commercial use.[12] Notably, resulting from the aforementioned inductive effect, the higher operating voltage of phosphate vanadates than that of vanadium oxides is one attracting merit of phosphate vanadium. The most feasible homologue of vanadium phosphate is VOPO₄, since it doesn't contain many more unwanted elements like Na or K when used in AZIBs (which means no pre-desodation or pre-depotassiation is required). VOPO₄·2H₂O with high operating voltage has become a competitive material, and the interlayer spacing can be widened through pre embedding engineering to improve the

*a*Key Laboratory of Hydraulic Machinery Transients, Ministry of Education, School of Power and Mechanical Engineering, Wuhan University, Wuhan 430072, China. E-mail: zxchen_pmc@whu.edu.cn; dingmy@whu.edu.cn

*b*College of Chemistry and Molecular Sciences, Wuhan University, Wuhan 430072, China. E-mail: joy_pu@whu.edu.cn

† Electronic supplementary information (ESI) available: Structural models, SEM images, CV curves, GCD curves and DOS. See DOI: https://doi.org/10.1039/d3sc02382f

zinc storage performance. However, despite measures like introducing metal ions (such as $K^+$, $Zn^{2+}$)[13,14] or small organic molecules (such as phenylamine, polypyrrole)[15,16] into the layers to adjust the interlayer spacing or stabilize the structure, the capacity of this material is far from reaching the theoretical capacity in the presented reports. Meanwhile, the dissolution of V is still a sticky issue even though high-cost super-concentration electrolytes or organic electrolytes are incorporated.[17]

Alternatively, multiple phases of vanadyl phosphates have been reported in addition to layered $VOPO_4 \cdot 2H_2O$, including $\alpha_I$, $\alpha_{II}$, $\beta$, $\gamma$, $\delta$, $\varepsilon$, $\omega$ (Fig. S1†), among which some phases have been studied tentatively as cathode materials in Li-ion and Na-ion batteries,[18–26] yet their zinc storage properties are not clear in aqueous batteries. Herein, we successfully synthesize $\delta$-$VOPO_4$ and measured its electrochemical performance in aqueous zinc-ion batteries. Compared to the performance of other phases of $VOPO_4$ in aqueous zinc-ion batteries, the delta-phase sample shows a higher operating voltage and satisfactory specific capacity (Fig. S2†). Results show that the $\delta$-$VOPO_4$ in platelet-like form displays a desirable capacity (90.88 mA h $g^{-1}$ at 10C, 1C = 330 mA $g^{-1}$) and high discharge voltage (1.46 V $vs.$ $Zn^{2+}$/Zn), laying a simple but strong foundation to exploit advanced ensuing AZIBs with high energy density without introducing complex doping or substitution groups.

## Experimental

### Synthesis

Various phases of vanadyl phosphates ($VOPO_4$) were prepared according to the methods reported in the literature.[17] In a typical process, $\delta$-$VOPO_4$ was prepared by a two-step method. First, $VOPO_4 \cdot 2H_2O$ (1 g) and isopropyl alcohol (14 mL) were first transferred to a Teflon-lined stainless-steel autoclave (50 mL) followed by keeping under 130 °C for 24 h. After washing with isopropyl alcohol several times and vacuum-drying at 110 °C, the powder was calcined at 600 °C for 14 h in a Muffle furnace to obtain $\delta$-$VOPO_4$.

### Characterization

The phases of powder materials were studied by X-ray diffraction (Rigaku MiniFlexll with Cu K$\alpha$ radiation ($k = 1.5408$ Å)) at a scan rate of 2° $min^{-1}$. The structure morphologies were studied by scanning electron microscopy (SEM, Zeiss Merlin Compact) and transmission electron microscopy (TEM, JEM-2100 Plus, JEOL). Energy dispersive spectroscopy (EDS) paired with SEM mapping was used to investigate the element distribution of the samples. An inductively coupled plasma optical emission spectrometer (ICP-OES, Agilent 5800) was used to determine the element ratio. An X-ray Photoelectron Spectrometer (XPS, ESCALAB250Xi, Thermo Fisher Scientific) was used to reveal the existing forms of element valence states within samples. Further information on the chemical bonding is revealed by means of a Fourier transform infrared spectrometer (FTIR, NICOLET 5700) and Raman spectrometer (DXR2, Thermo Fisher).

### Electrochemical measurements

Electrochemical tests of all the electrodes were performed with CR2032 coin-type cells with Zn foil as the counter electrode. The working electrode was fabricated using a slurry of active material, Super P, and PTFE (poly-tetrafluoroethylene) in a weight ratio of 6 : 2 : 2 with isopropyl alcohol as a humectant. The slurry was coated onto a Ti mesh and dried at 80 °C in a vacuum oven for 12 h. A glass fiber membrane was used as the separator and 3 m $Zn(CF_3SO_3)_2$ was prepared as the electrolyte. The electrochemical performance of the battery was evaluated using a LAND battery test system (CT2001A) including galvanostatic charge–discharge (GCD), rate and long-term cycling performance. The galvanostatic intermittent titration technique (GITT) was performed under a modified GCD mode, in which an operation period includes two parts: a charge/discharge procedure lasting for 10 min at 50 mA $g^{-1}$ and a subsequent pause time for 30 min. Cyclic voltammetry (CV) tests at different scan rates were performed on an electrochemical workstation (Corrtest, CS350H).

### Computational methods

First-principles calculations were carried out using density functional theory (DFT) with the projector augmented-wave method as implemented using the Vienna *Ab initio* Simulation Package (VASP) code. The Perdew–Burke–Ernzerhof (PBE) of generalized gradient approximation (GGA) was chosen for the exchange–correction functional. Hubbard corrections to intra-atomic coulombic repulsion were considered and the effective Hubbard $U$ parameters to 4.5 eV for V were set to correct electron–electron interactions of V 3d electrons.[27–29] The wave functions were expanded based on plane-waves with the energy cutoff set to 600 eV. All lattice parameters and atomic sites were fully optimized until the change of the total energy and residual forces were less than $10^{-5}$ eV and 0.02 eV $Å^{-1}$, respectively. A $1 \times 1 \times 1$ supercell containing 8 V and 8 P and 40 O atoms was considered for exploring the energies of different configurations taking up Zn ions. A $\Gamma$-centered $5 \times 5 \times 5$ $k$-point mesh with a reciprocal space was employed in the Brillouin zone of the supercell. The equilibrium voltage is evaluated using the internal energies from the DFT calculations according to the following equation:

$$V = \frac{E(Zn_{x_1}VOPO_4) - E(Zn_{x_2}VOPO_4) - (x_2 - x_1)E(Zn)}{2(x_2 - x_1)F}$$

where $F$ is the Faraday constant and $E(Zn_{x_1}VOPO_4)$, $E(Zn_{x_2}$-$VOPO_4)$ and $E(Zn)$ are the internal energies at 0 K, respectively.

## Results and discussion

### Derivation and characterization of $\delta$-$VOPO_4$

Scanning electron microscopy (SEM) was performed to track the morphology evolution during the preparation process. $\delta$-$VOPO_4$ prepared herein can be described as aggregates of micron-sized platelets in Fig. 1a and b. Such a morphology is similar to the flaky appearance of its precursors ($VOPO_4 \cdot 2H_2O$ and $VOHPO_4 \cdot 0.5H_2O$) shown in Fig. S3a and b.† Compared
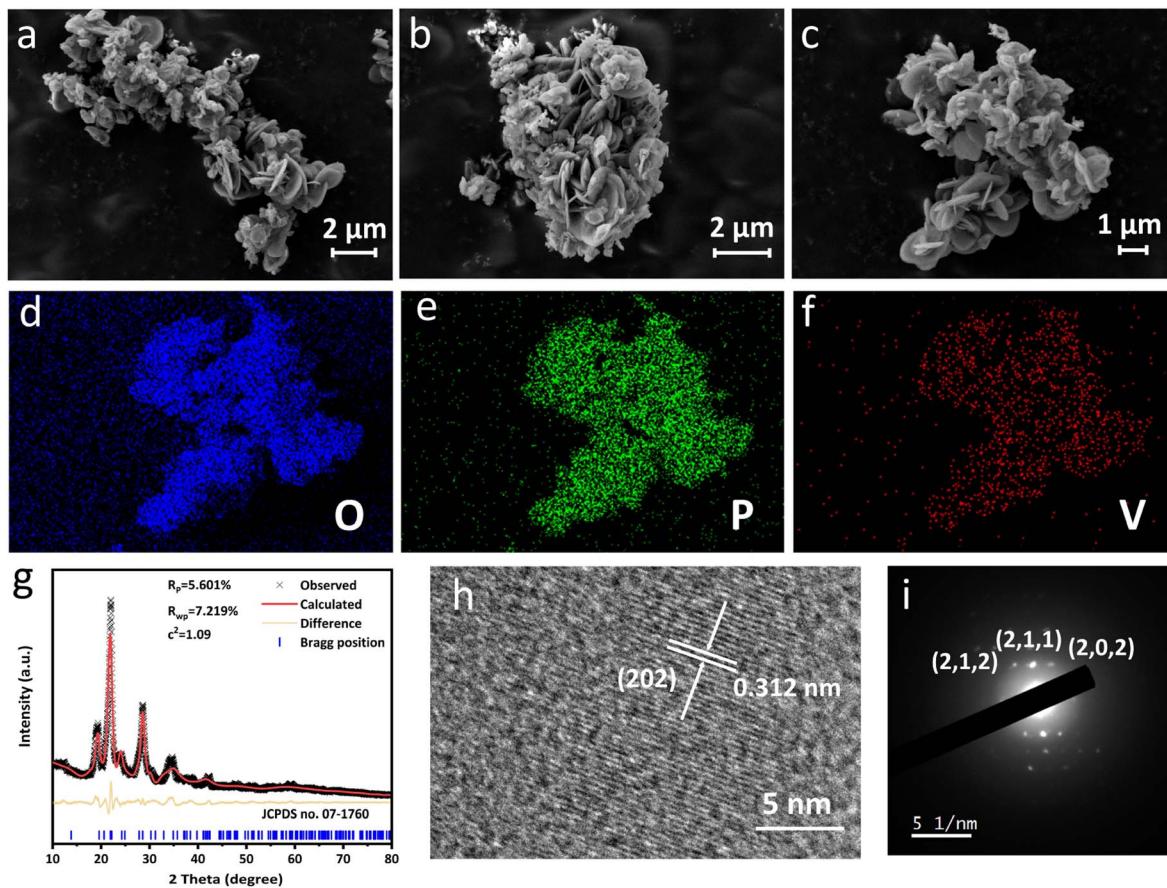
Fig. 1 (a–c) SEM images, (d–f) elemental mappings, (g) Rietveld XRD pattern, (h) HR-TEM and (i) SAED images of δ-VOPO$_4$.

with VOPO$_4$·2H$_2$O consisted of dense massive flakes, the units of δ-VOPO$_4$ are smaller in diameter and less tightly stacked with each other, and the gap in the framework can provide more contact area for the material and the electrolyte, which is beneficial for performance. The elemental mappings displayed in Fig. 1d–f show that the V, O and P elements are homogeneously distributed in the sample. The XRD pattern of δ-VOPO$_4$ was refined according to the standard card (JCPDS no. 07-1760). The Rietveld refinement in Fig. 1g confirms that the crystal structure of δ-VOPO$_4$ is indexed to a space group

of tetragonal $P4_2/mbc$, and the unit cell parameters are identified as $a = b = 9.2016$ Å, and $c = 8.4953$ Å. The fitting was satisfactory ($R_{wp} = 5.601\%$, $R_p = 7.219\%$). The high-resolution transmission electron microscopy (HRTEM) image of δ-VOPO$_4$ shown in Fig. 1h exhibits lattice fringes with a spacing of 0.312 nm corresponding to the (202) planes. Selected-area electron diffraction (SAED) patterns (Fig. 1i) observed from the flakes in a normal direction can be well indexed to the (212), (211) and (202) projection of δ-VOPO$_4$.
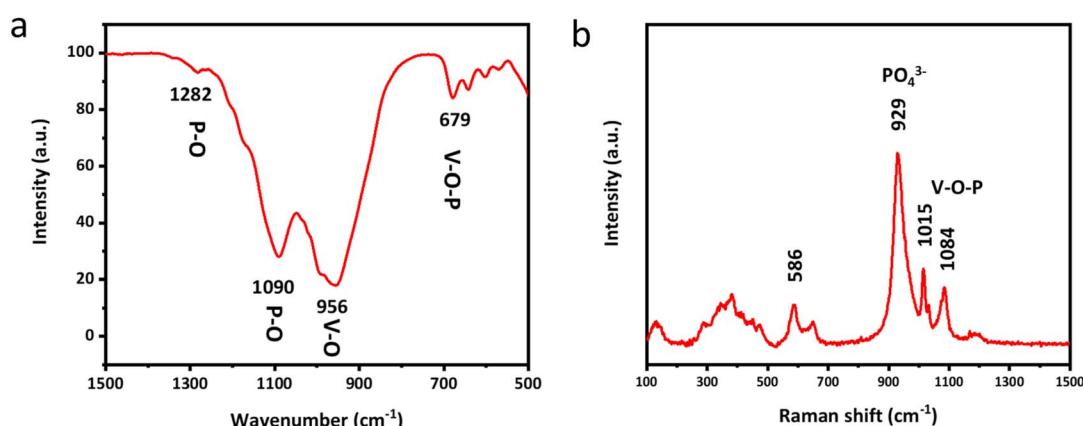


Fig. 2 (a) FTIR spectra and (b) Raman spectra of δ-VOPO$_4$ powder.

Fourier transform infrared spectroscopy (FTIR) and Raman spectroscopy are subsequently employed to clearly unveil the molecular structure and chemical composition of δ-VOPO₄. As shown in Fig. 2a, the V–O–P bending vibration peak is located at 679 cm⁻¹. The peaks located in the range of 1000 cm⁻¹ to 1250 cm⁻¹ can be attributed to P–O stretching vibration modes in the (PO₄) group, while the peak at 1630 cm⁻¹ of the sample corresponds to H–O–H bending vibrations due to adsorbed water on the surface of the material.[30] Raman spectroscopy can also convey the same information as depicted in Fig. 2b. The

peak at 941 cm⁻¹ in δ-VOPO₄ can be attributed to O–P–O stretching modes. The peaks of V=O stretching vibration and V–O–P coupled stretching in δ-VOPO₄ are located respectively at 1015 cm⁻¹ and 1084 cm⁻¹.

## Zn²⁺ storage performance of δ-VOPO₄

In light of the merits described above, we paid special attention to the electrochemical properties of different phases in AZIBs. Compared to the layered dihydrate phase with average voltage
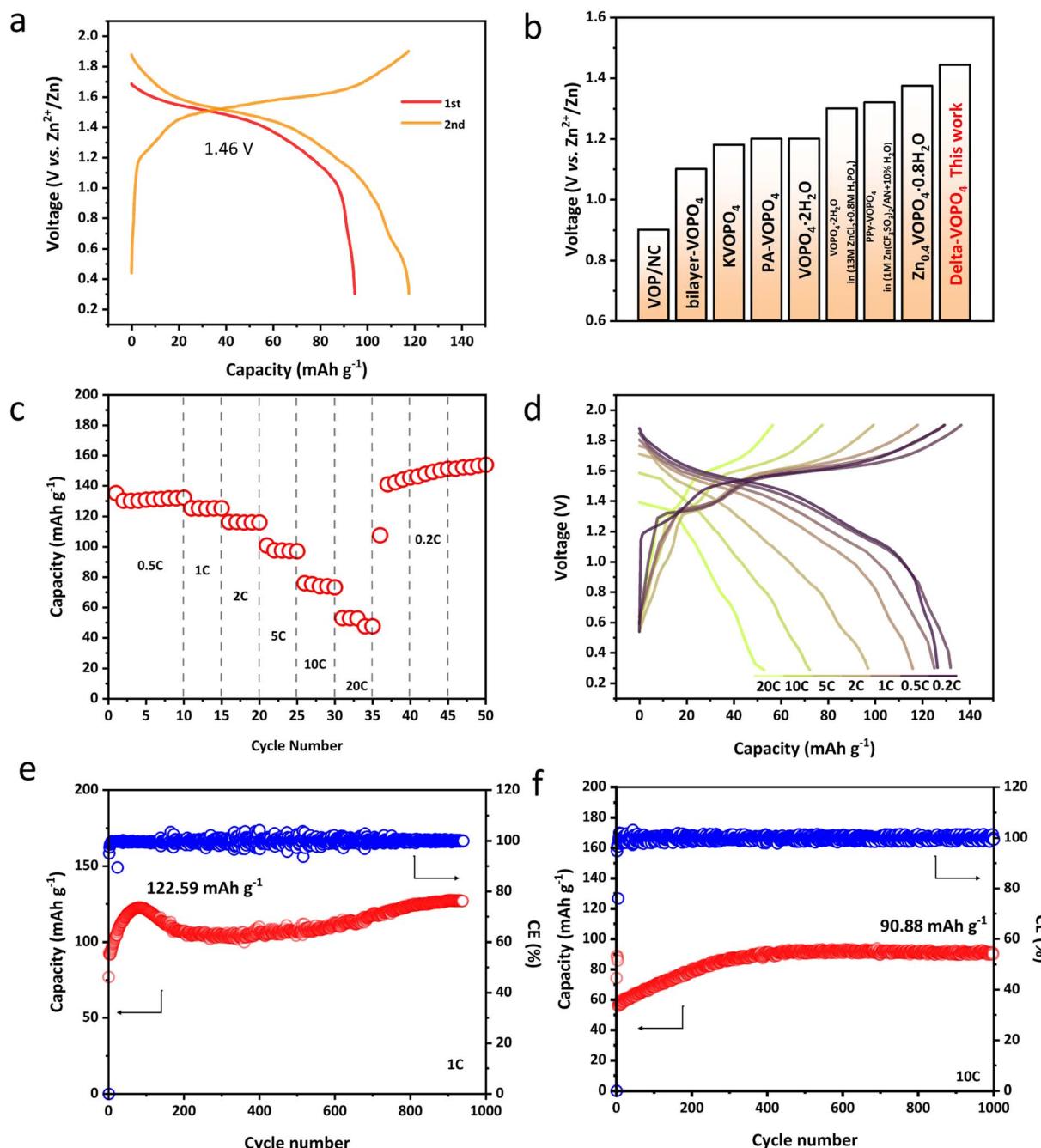


**Fig. 3** (a) The first two discharge/charge curves of δ-VOPO₄; (b) the average discharge voltage of reported VOPO₄ materials[13–17,37,38] and this work; (c) rate performances of δ-VOPO₄ at different current densities; (d) charge/discharge curves of δ-VOPO₄ at different current densities; cycling performance of δ-VOPO₄ at 1C (330 mA g⁻¹) (e) and 10C (3300 mA g⁻¹) (f).

only around 1.2 V *vs.* $Zn^{2+}/Zn$, $\delta$-$VOPO_4$ has witnessed an elevated operating voltage of 1.46 V as shown in Fig. 3a. The charge–discharge behaviour of $\delta$-$VOPO_4$ can be seen through the comparison of the CV tests at the scan rate of 0.1 mV s$^{-1}$ in the voltage range of 0.3–1.9 V as shown in Fig. S4a.[†][31] $\delta$-$VOPO_4$ has a pair of major oxidation/reduction peaks at 1.63 V and 1.51 V corresponding to the redox couple of $V^{5+}/V^{4+}$. A single major redox peak proves that the material has fewer phase transitions and the capacity is concentrated at high voltages, providing higher energy densities. Meantime, $\delta$-$VOPO_4$ exhibits a discharge capacity of 94.8 mA h g$^{-1}$ at 0.1C (1C = 330 mA g$^{-1}$) in the initial cycle and 117.8 mA h g$^{-1}$ in the second cycle with nearly 100% coulombic efficiency. The average discharge voltage of the delta-phase is also in the leading position among the various reported vanadium phosphate materials as displayed in Fig. 3b. Owing to the micron-sized platelets with limited diameter and stronger induction effect, the as prepared $\delta$-$VOPO_4$ sample shows an excellent rate performance as revealed in Fig. 3c and d. In particular, it provides 126.6, 132.2, 125.3, 116.1, 97.1, 73.3 and 53 mA h g$^{-1}$ at 0.2C, 0.5C, 1C, 2C, 5C, 10C and 20C respectively. When the current density comes back to 0.2C, the battery can still deliver the ideal capacity stably. The capacity of $\delta$-$VOPO_4$ slowly rises to 122.6 mA h g$^{-1}$ at a current density of 1C and keeps stable after 940 cycles (Fig. 3e). The rise of the capacity is related to the typical activation process, which was commonly observed for multivalent metal-ion batteries in many previous studies.[32–34] What is more impressive is the long-term cycle performance at the high current density displayed in Fig. 3f and g. When the current density is increased to 10C (3300 mA g$^{-1}$), $\delta$-$VOPO_4$ still exhibits an inspiring high reversible capacity of 90.9 mA h g$^{-1}$. The corresponding charge–discharge profiles of the $\delta$-$VOPO_4$ cathode are displayed in Fig. S5.[†] It can be seen that the average discharge voltage at 1 A g$^{-1}$ drops from 1.46 V to 1.32 V after 300 cycles. The voltage decay is much smaller than that of other V-based polyanionic cathodes in ZIBs, such as $Li_3V_2(PO_4)_3$, $Na_3V_2(PO_4)_3$, and $Na_3V_2(PO_4)_2F_3$.[35,36] Note that the GCD profiles almost kept unchanged at 10 A g$^{-1}$, and a high operating voltage of 1.36 V was still retained after 1000 cycles, demonstrating an outstanding operating voltage retention.

The reason behind such excellent kinetics can be explained by the galvanostatic intermittent titration technique (GITT) to distinguish the ion mobility in Fig. S6[†] and as a result, an overwhelming $Zn^{2+}$ diffusion coefficient of $10^{-10}$ cm$^{-2}$ s$^{-1}$ has been detected in the $\delta$-$VOPO_4$. To confirm the kinetics, Cyclic Voltammetry (CV) under various scan rates was performed to further explore the electrochemical kinetics of $Zn^{2+}$ storage performance as depicted in Fig. S4b–d.[†] The energy storage process can be distinguished based on the power-law relationship between peak currents ($i$) and scan rate ($v$) ($i = av^b$) just as described in the reported literature. Parameters $a$ and $b$ are constants that can be calculated from $\log(v)$ *vs.* $\log(i)$. When $b = 0.5$ it is ascribed to the diffusion-controlled process and when $b = 1$ it corresponds to capacitive behaviour. The fitted slope values ($b$) for the two main redox peaks are calculated as 0.757 and 0.899, indicating fast $Zn^{2+}$ diffusion kinetics in the $\delta$-$VOPO_4$ electrode.

## $Zn^{2+}$ storage mechanism of $\delta$-$VOPO_4$

The change of the vanadium valence state from the initial voltage to the cut-off voltage is analysed using XPS spectra for samples at different states of charge (SOC) as shown in Fig. 4a. It's clearly shown that the valence states of vanadium in the prepared samples are dominated by $V^{5+}$, consistent with our designed formula. When discharged to 0.3 V, the valence state of V is reduced along with the intercalation of $Zn^{2+}$ and thus both $V^{3+}$ and $V^{4+}$ are observed. Conversely, vanadium has been oxidized to $V^{4+}$ and $V^{5+}$ during $Zn^{2+}$ extraction from the structure when recharging to 1.9 V. Notably, the combination of $V^{4+}$ and $V^{5+}$ at the charged state indicates there was Zn residual. This hypothesis could be validated by Inductively coupled plasma optical emission spectrometer (ICP-OES) measurements shown in Fig. 4b. When discharging from the open-circuit voltage of 1.68 V of the pristine state to 0.3 V, the ratio of Zn : V : P is calculated as 0.51 : 1 : 1. When charged to 1.9 V, the molar ratio of Zn : V : P is 0.13 : 1 : 1, indicating $Zn^{2+}$ residual and agreeing with the above XPS test result.

*Ex situ* XRD was carried out to investigate the phase changes of $\delta$-$VOPO_4$ during the discharging and charging process. As displayed in Fig. S7,[†] the typical peaks such as (201) and (202) have experienced a reversible shift during the $Zn^{2+}$ intercalation/deintercalation, indicating a topological $Zn^{2+}$ insertion/extraction into/from the lattice. Calculated based on the *ex situ* XRD pattern, the volume change of $\delta$-$VOPO_4$ is only 1.1% after fully intercalating $Zn^{2+}$, which is essential for its prolonged cycle life. Besides, two new peaks located at 31.2° and 32.8° emerged during discharging and disappeared upon charging, which was related to the formation of partially hydrated phosphate on the surface of the electrode. Generally, the main crystal structure of $\delta$-$VOPO_4$ was still maintained upon discharging and charging, which can account for the outstanding capacity and operating voltage retention in Fig. 3 and S5.[†]

Moreover, more information about the molecular structure can be concluded from *ex situ* Raman spectra displayed in Fig. 4c to unveil the $Zn^{2+}$ storage mechanism in $\delta$-$VOPO_4$. In the process of $Zn^{2+}$ insertion, Zn forms coordination with the O atom from the $PO_4$ group, resulting in the deformation of the $PO_4$ structure and the weakening and shift of the Raman intensity. When the $Zn^{2+}$ is deintercalated, the P–O bond gets stronger and shorter due to the increased Coulomb force. The intensity of the Raman characteristic peak of $PO_4^{3-}$ recovers, indicating the stability of the structure of $PO_4$ groups during the (de)intercalation of $Zn^{2+}$.

To further reveal the fundamental mechanisms of $\delta$-$VOPO_4$, theoretical calculation with density functional theory (DFT) was used to establish the structural models of $\delta$-$VOPO_4$ before and after zincification as illustrated in Fig. 5a. When became fully zincified, each unit cell is able to store eight Zn atoms corresponding to the chemical formula $ZnVOPO_4$, corresponding to a theoretical capacity of over 300 mA h g$^{-1}$. The chemical coordination environment of all the Zn is the same. However, in fact, none of the reported vanadium phosphate ($VOPO_4$) materials have achieved such high specific capacity due to the unstable structure.
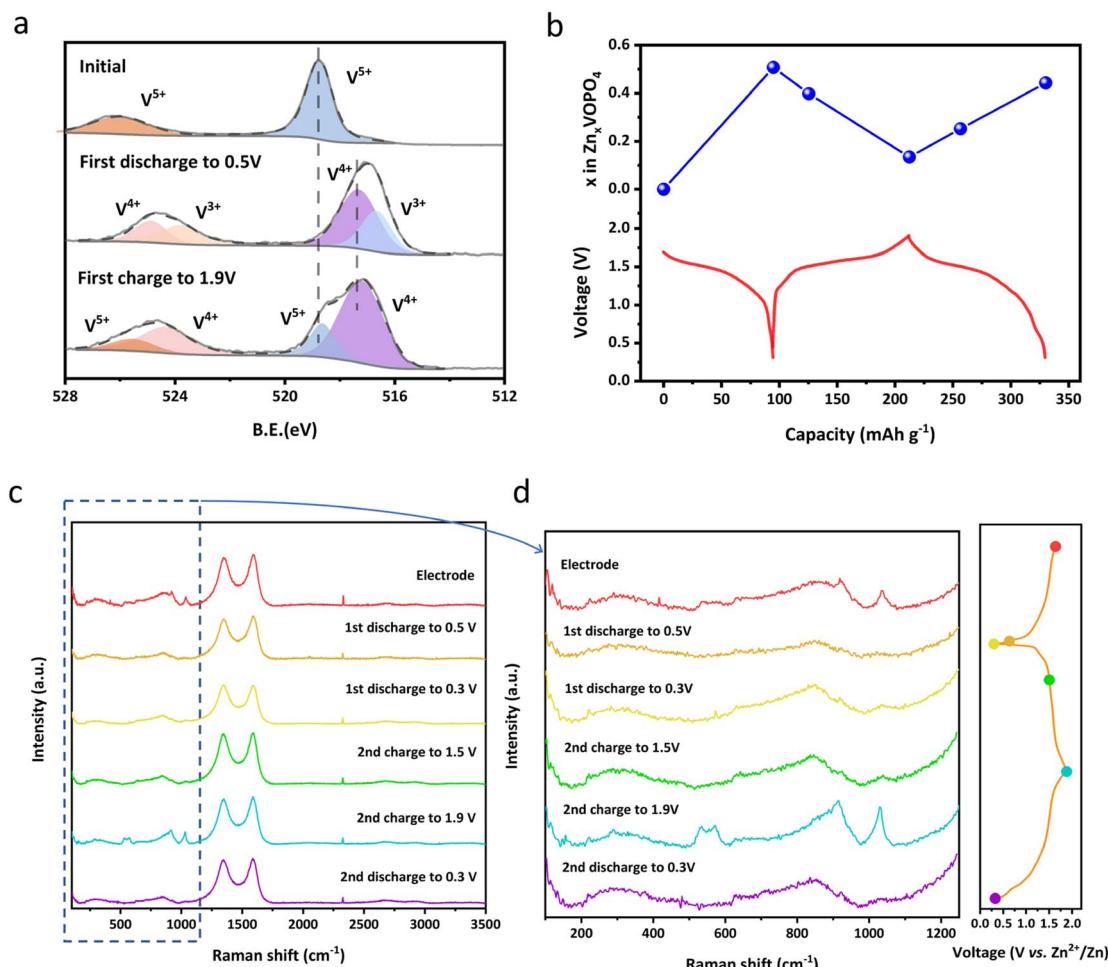
**Fig. 4** (a) *Ex situ* XPS spectra of V 2p of δ-VOPO$_4$; (b) *ex situ* ICP measurement of δ-VOPO$_4$ during the first two cycles; (c and d) *ex situ* Raman spectra of δ-VOPO$_4$ during the first two cycles.

In this work, due to the ICP measurements, 0.5 Zn$^{2+}$ can be intercalated per δ-VOPO$_4$. As depicted in Fig. 5b, the DFT calculation results illuminate that the equilibrium voltage is 1.47 V at $0 \leq x \leq 0.5$ and 1.45 V at $0.5 \leq x \leq 0.625$ corresponding to the V$^{5+}$/V$^{4+}$ and V$^{4+}$/V$^{3+}$ redox couples, respectively, which agree well with the experimental results. First, the high potential is brought about by the "inductive effect" of strong P–O covalent bonds that drive the electron density away from the V center in the V–O–P layers, thus weakening the covalence of the V–O bonds, and leading to the higher operating voltage. Second, the unique structure and V···O contact are the key factors for its high voltage and excellent Zn$^{2+}$ storage performance. The structure of δ-VOPO$_4$ contains infinite polar chains of trans-corner sharing VO$_6$ octahedra with the [V=O···V=O···]$_\infty$ backbone. Girgsdies *et al.* found that the V···O contact length of δ-VOPO$_4$ reached 3.1 Å, which was significantly longer than that of other VOPO$_4$ phases.[39] In addition, the O=V···O angle is 168°, which obviously deviates from more or less straight arrangement compared with other VOPO$_4$ phases. The unique structural distortion indicates that vanadium in δ-VOPO$_4$ has higher redox activity and potential. There is also a lower plateau at 0.69 V, which may be associated with the insertion of Zn$^{2+}$ into different sites of δ-VOPO$_4$.

The total density of states (DOS) of δ-VOPO$_4$ was calculated to further illuminate the bonding condition of the structure (Fig. S8†). shows that the O-2p and P-2p orbitals are clearly overlapped corresponding to the (PO$_4$)$^{3-}$ group. The strong overlapping of the V-3p orbitals and the O-2p orbitals shows the strong covalent bond between V and O atoms. It is observed at the valence band position in Fig. S9† that the area variation of state density before and after zinc insertion is mainly concentrated between −4.45 eV ($\varepsilon_0$) and the Fermi level because the integration below −4.45 eV has no change before and after zincification. Through integration, it can be deduced that the intercalation of Zn mainly affects the density of states in this region, and only the integral value of V has been changed proving that the electrons supplied by Zn$^{2+}$ are completely added to the V-3d orbital, so that V is the redox centre of the material.[40] In order to elucidate the interaction between different atoms, the Bader charge population of δ-VOPO$_4$ before and after zincification is calculated in Fig. 5d. During zincification, due to the charge compensation, the Bader net charge of the V atom has been reduced as the redox center. The net charge of the O atom has an evident increase close to the absolute value of formal charge (−2), implying that there is a strong ionic bond
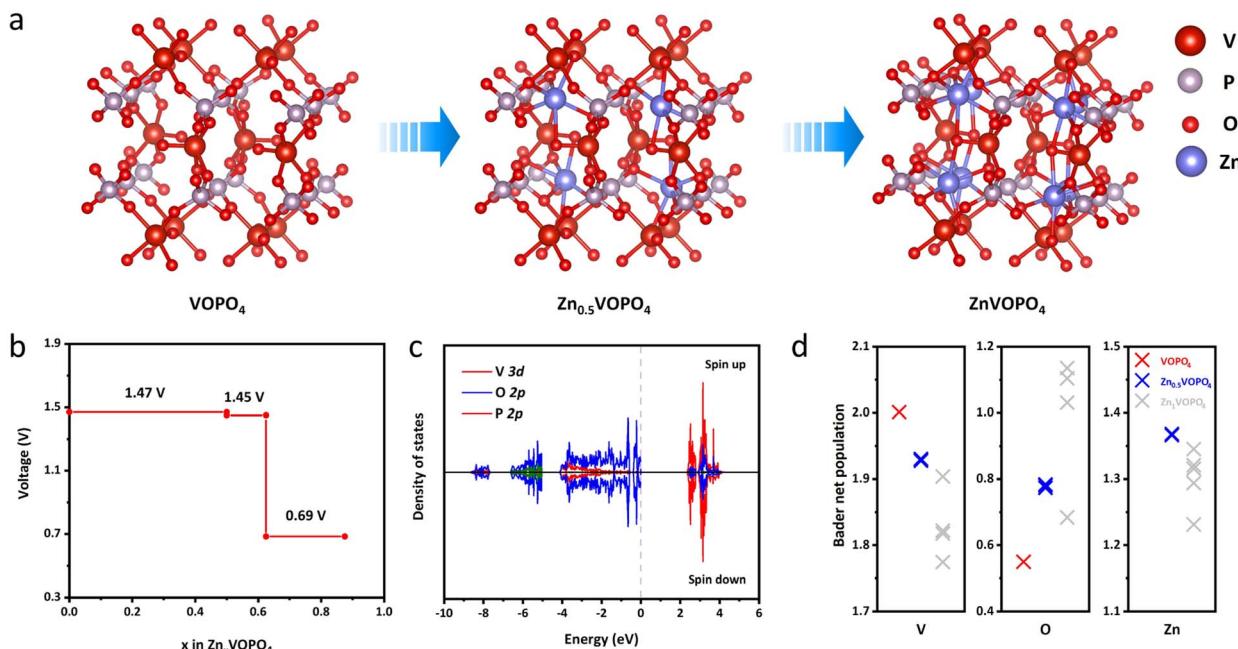
Fig. 5 (a) The schematic illustration of structural models of δ-VOPO$_4$ before and after dezincification; (b) the equilibrium reaction voltage profiles predicted with DFT calculations; (c) the density of states (DOS) of δ-VOPO$_4$; the Fermi energy level is set to zero; (d) the Bader charge analysis of δ-VOPO$_4$.

between Zn and O. Similarly, the net charge of Zn is close to the formal charge (+2), indicating that the Zn–O bond is more like an ionic bond. Obviously, the ionic character of the Zn–O bond may significantly raise the $V^{n+}/V^{(n+1)+}$ redox potential as a primary inductive effect.

## Conclusions

A novel polyanionic delta oxovanadium phosphate (δ-VOPO$_4$) is synthesized without complex pre-intercalation of metal elements/small molecules, and employed as a cathode in aqueous zinc-ion batteries. Superior to various vanadyl phosphates with a similar chemical composition, it displays a high average discharge voltage of 1.46 V, and an impressive long-term cycling performance at 1C and 10C. This work assuredly illustrates that the performance could be enhanced by structure optimization and phase transition, which may shed new insights to exploit alternative cathodes out of vanadyl phosphate families for zinc-ion batteries.

## Data availability

The authors declare that all data supporting the findings of this study are available from the corresponding author upon reasonable request.

## Author contributions

Dong Zhao: data curation, formal analysis, investigation, writing – original draft, writing – review & editing. Xiangjun Pu: investigation, writing – original draft, writing – review & editing.

Shenglong Tang: data curation, methodology. Mingyue Ding: supervision, writing – original draft. Yubin Zeng: methodology, writing – review & editing. Yuliang Cao: funding acquisition, writing – review & editing. Zhongxue Chen: supervision, funding acquisition, writing – review & editing.

## Conflicts of interest

There are no conflicts to declare.

## Acknowledgements

## References

1 Y. Cao, M. Li, J. Lu, J. Liu and K. Amine, *Nat. Nanotechnol.*, 2019, **14**, 200–207.

2 Z. Lin, T. Liu, X. Ai and C. Liang, *Nat. Commun.*, 2018, **9**, 5262.

3 D. Zhao, C. Wang, Y. Ding, M. Ding, Y. Cao and Z. Chen, *ChemSusChem*, 2022, **15**, 202200479.

4 Y. Tian, G. Zeng, A. Rutt, T. Shi, H. Kim, J. Wang, J. Koettgen, Y. Sun, B. Ouyang, T. Chen, Z. Lun, Z. Rong, K. Persson and G. Ceder, *Chem. Rev.*, 2021, **121**, 1623–1669.

5 S. Chen, D. Zhao, L. Chen, G. Liu, Y. Ding, Y. Cao and Z. Chen, *Small Struct.*, 2021, **2**, 2100082.

6 C. Dong, F. Xu, L. Chen, Z. Chen and Y. Cao, *Small Struct.*, 2021, **2**, 2100001.

7 D. Zhao, S. Chen, Y. Lai, M. Ding, Y. Cao and Z. Chen, *Nano Energy*, 2022, **100**, 107520.

8 H. Li, S. Liu, T. Yuan, B. Wang, P. Sheng, L. Xu, G. Zhao, H. Bai, X. Chen, Z. Chen and Y. Cao, *Acta Phys.-Chim. Sin.*, 2021, **37**, 1907049.

9 S. Tang, C. Wang, X. Pu, X. Gu and Z. Chen, *Acta Phys.-Chim. Sin.*, 2023, **39**, 2212037.

10 Z. Wu, F. Ye, Q. Liu, R. Pang, Y. Liu, L. Jiang, Z. Tang and L. Hu, *Adv. Energy Mater.*, 2022, **12**, 2200654.

11 F. Ye, R. Pang, C. Lu, Q. Liu, Y. Wu, R. Ma and L. Hu, *Angew. Chem., Int. Ed.*, 2023, **62**, e202303480.

12 X. Pu, H. Wang, D. Zhao, H. Yang, X. Ai, S. Cao, Z. Chen and Y. Cao, *Small*, 2019, **15**, 1805427.

13 K. Zhu, Z. Sun, P. Liu, H. Li, Y. Wang, K. Cao and L. Jiao, *J. Energy Chem.*, 2021, **63**, 239–245.

14 Z. Wu, Y. Wang, L. Zhang, L. Jiang, W. Tian, C. Cai, J. Price, Q. Gu and L. Hu, *ACS Appl. Energy Mater.*, 2020, **3**, 3919–3927.

15 L. Hu, Z. Wu, C. Lu, F. Ye, Q. Liu and Z. Sun, *Energy Environ. Sci.*, 2021, **14**, 4095–4106.

16 V. Verma, S. Kumar, W. Manalastas, J. Zhao, R. Chua, S. Meng, P. Kidkhunthod and M. Srinivasan, *ACS Appl. Energy Mater.*, 2019, **2**, 8667–8674.

17 H. Y. Shi, Y. Song, Z. Qin, C. Li, D. Guo, X. X. Liu and X. Sun, *Angew. Chem., Int. Ed.*, 2019, **58**, 16057–16061.

18 B. M. Azmi, T. Ishihara, H. Nishiguchi and Y. Takita, *Electrochim. Acta*, 2002, **48**, 165–170.

19 B. M. Azmi, T. Ishihara, H. Nishiguchi and Y. Takita, *J. Power Sources*, 2003, **119–121**, 273–277.

20 Z. Chen, Q. Chen, H. Wang, R. Zhang, H. Zhou, L. Chen and M. S. Whittingham, *Electrochem. Commun.*, 2014, **46**, 67–70.

21 N. Dupré, G. Wallez, J. Gaubicher and M. Quarton, *J. Solid State Chem.*, 2004, **177**, 2896–2902.

22 Y.-C. Lin, M. F. V. Hidalgo, I.-H. Chu, N. A. Chernova, M. S. Whittingham and S. P. Ong, *J. Mater. Chem. A*, 2017, **5**, 17421–17431.

23 M. Zhang, S. Zhang, H. Gao, F. L. Meng and C. Deng, *J. Electroanal. Chem.*, 2014, **713**, 119–124.

24 Y. Fang, Q. Liu, L. Xiao, Y. Rong, Y. Liu, Z. Chen, X. Ai, Y. Cao, H. Yang, J. Xie, C. Sun, X. Zhang, B. Aoun, X. Xing, X. Xiao and Y. Ren, *Chem*, 2018, **4**, 1–14.

25 L. Zhang, X. Hu, Y. Wu, Y. Gao, C. Lin, C. Dong, G. Li, F. Xu, S. Zhang and K. Zhang, *Mater. Today Energy*, 2021, **21**, 100756.

26 H. Y. Shi, Z. Jia, W. Wu, X. Zhang, X. X. Liu and X. Sun, *Chem.–Eur. J.*, 2020, **26**, 8190–8204.

27 Q. Bai, L. Yang, H. Chen and Y. Mo, *Adv. Energy Mater.*, 2018, **8**, 1702998.

28 A. Jain, G. Hautier, C. J. Moore, S. Ping Ong, C. C. Fischer, T. Mueller, K. A. Persson and G. Ceder, *Comput. Mater. Sci.*, 2011, **50**, 2295–2310.

29 G. Kresse and J. Furthmüller, *Phys. Rev. B: Condens. Matter Mater. Phys.*, 1996, **54**, 11169–11186.

30 P. Mei, Y. V. Kaneti, M. Pramanik, T. Takei, Ö. Dag, Y. Sugahara and Y. Yamauchi, *Nano Energy*, 2018, **52**, 336–344.

31 X. Pu, D. Zhao, C. Fu, Z. Chen, S. Cao, C. Wang and Y. Cao, *Angew. Chem., Int. Ed.*, 2021, **60**, 21310–21318.

32 F. Ming, H. Liang, Y. Lei, S. Kandambeth, M. Eddaoudi and H. N. Alshareef, *ACS Energy Lett.*, 2018, **3**, 2602–2609.

33 C. E. M. Lewis, J. F. S. Fernando, D. P. Siriwardena, K. L. Firestein, C. Zhang, J. E. Treifeldt and D. V. Golberg, *Adv. Mater. Technol.*, 2021, **7**, 2100505.

34 H. Liu, L. Jiang, B. Cao, H. Du, H. Lu, Y. Ma, H. Wang, H. Guo, Q. Huang, B. Xu and S. Guo, *ACS Nano*, 2022, **16**, 14539–14548.

35 C. Li, W. Yuan, C. Li, H. Wang, L. Wang, Y. Liu and N. Zhang, *Chem. Commun.*, 2021, **57**, 4319–4322.

36 W. Li, X. Jing, K. Jiang and D. Wang, *ACS Appl. Energy Mater.*, 2021, **4**, 2797–2807.

37 L. Ou, Z. Liu, Y. Zhou, H. Ou, J. Zhu, X. Cao, G. Fang, J. Zhou and S. Liang, *Chem. Eng. J.*, 2021, **426**, 131868.

38 Z. Wu, C. Lu, F. Ye, L. Zhang, L. Jiang, Q. Liu, H. Dong, Z. Sun and L. Hu, *Adv. Funct. Mater.*, 2021, **31**, 2106816.

39 F. Girgsdies, M. Schneider, A. Brückner, T. Ressler and R. Schlögl, *Solid State Sci.*, 2009, **11**, 1258–1264.

40 R. Lian, D. Wang, X. Ming, R. Zhang, Y. Wei, J. Feng, X. Meng and G. Chen, *J. Mater. Chem. A*, 2018, **6**, 16228–16234.